Surface explosion and subsequent core expansion of laser-heated clusters probed by time-resolved photoelectron spectroscopy

Akinobu Niozu [1,2] Hironobu Fukuzawa [3,4] Toru Hagiya,[1] Akifumi Yamamoto,[1] Daehyun You,[3] Shu Saito,[3]
Yudai Ishimura,[3] Tadashi Togashi [4,5] Shigeki Owada [4,5] Kensuke Tono [4,5] Makina Yabashi [4,5] Shin-ichi Wada [2]
Kazuhiro Matsuda [1,6] Kiyoshi Ueda [3,4] and Kiyonobu Nagaya[1,4]

[1]*Department of Physics, Kyoto University, Kyoto 606-8502, Japan*
[2]*Graduate School of Advanced Science and Engineering, Hiroshima University, Higashi-hiroshima 739-8526, Japan*
[3]*Institute of Multidisciplinary Research for Advanced Materials, Tohoku University, Sendai 980-8577, Japan*
[4]*RIKEN SPring-8 Center, Sayo, Hyogo 679-5148, Japan*
[5]*Japan Synchrotron Radiation Research Institute (JASRI), Sayo, Hyogo 679-5198, Japan*
[6]*Department of Physics, Kumamoto University, Kumamoto 860-8555, Japan*

The dynamics of nanoplasma produced by an intense near-infrared pulse was investigated by time-resolved soft x-ray photoelectron spectroscopy. The pump-probe electron spectra indicate transient evolution of the electronic states of the constituent atoms and ions during plasma formation and disintegration. The delay dependence of photoelectron yields supports two-step fragmentation of laser-heated clusters, i.e., rapid explosion of surface ions followed by slow expansion of neutral atoms. The speed of the neutral core expansion was evaluated by comparing the experimental data with a model of uniform neutral core expansion.

I. INTRODUCTION

Over the past few decades, the interaction between matter and intense laser fields has been studied actively. Understanding the intense laser-matter interaction is of fundamental scientific interest and is important in various technological and medical applications of intense lasers, e.g., laser machining and medical surgery. Rare-gas clusters are a proven ideal test bed to investigate laser-matter interactions [1–3] because they have no energy dissipation into the surrounding media. The dynamics of a cluster in an intense near-infrared (NIR) laser field is of particular interest where the cluster can absorb the energy of the laser field in an efficient manner [3]. Here, upon strong NIR laser excitation, the cluster is ionized by multiphoton ionization or field ionization mechanisms and heated by collective heating. Most of the emitted electrons are trapped by the emerging Coulomb potential, which leads to the formation of a nanometer-sized plasma, i.e., the so-called nanoplasma.

Nanoplasma dynamics has primarily been studied by measuring energetic ions [1,2,4] and electrons [5,6] emitted from the heated nanoplasma. Pump-probe measurements with short laser pulses [5,7] have revealed the explosion dynamics of nanoplasma in greater detail on a picosecond timescale. Recent experiments suggest the formation of neutral atoms in the central part of nanoplasma [8–14] through efficient charge recombination during the nanoplasma expansion. The first studies of the recombination dynamics were carried out by pump-probe ion and electron spectroscopy using the reionization of excited atoms from recombination technique [10,12] where Rydberg atoms formed via recombination processes

are reionized with a probe optical laser pulse. In addition, the structural evolution of nanoplasmas produced by ionization of large Xe nanoparticles has been studied by time-resolved single-particle imaging [13,15], which was enabled by the availability of short-wavelength free-electron lasers (FELs) [16,17]. The time-resolved diffraction data provided evidence of the rapid surface explosion of nanoplasma [15] and the formation of residual cluster core at the nanosecond timescale after laser excitation [13].

X-ray photoelectron spectroscopy is a commonly used technique to probe the electronic states and chemical environment of matter. Particularly, time-resolved photoelectron spectroscopy (TRPES) [18] with short-wavelength FELs is a promising technique that can be used to characterize photoinduced dynamics in molecules and clusters with femtosecond temporal resolution. To date, FEL-based TRPES has been successfully employed to investigate photoinduced dynamics of organic molecules [19–21]. TRPES is effectively employed in the study of intense laser-cluster interactions because it can directly probe the transient electronic states in expanding clusters, including the dynamics of neutral atoms.

In this paper, we applied time-resolved photoelectron spectroscopy to investigate the evolution of the electronic state in the nanoplasma produced by an intense NIR laser pulse. Here, the electron energy levels in the expanding clusters were determined using short-wavelength ($h\nu = 135$ eV) and sufficiently intense FEL pulses as the probe. Using a recently developed temporal jitter correction tool [22,23] that realizes improved temporal resolution, we obtained the direct signatures of the electron trapping in the nanoplasma and surface ion explosion. In addition, we identified the slow expansion of
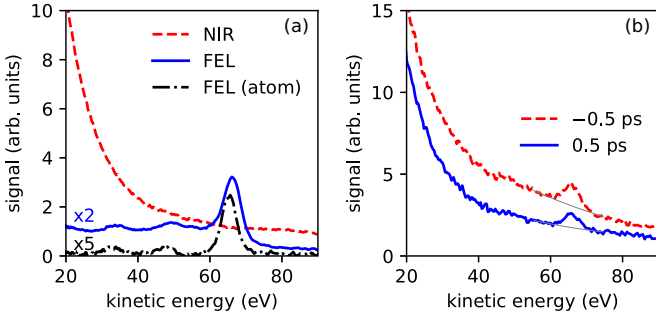
FIG. 1. (a) Electron kinetic-energy spectra from Xe clusters irradiated by NIR pulses, by FEL pulses, and from isolated Xe atoms irradiated by FEL. (b) Pump-probe electron spectra at delay -0.5 ps and 0.5 ps. The NIR intensity was 1.5×10^{14} W/cm^2.

the neutral cluster core on hundreds of picosecond timescales, which is more than one order of magnitude longer than that of ion explosion.

II. METHOD

A. Experiment

Experiments were performed at SACLA BL1 [24], and the details of the experimental setup are described in the literature [25,26]. FEL pulses with a photon energy of 135 eV and pulse duration of $\approx$30 fs [27] were attenuated using an Sn filter (thickness: 0.2 μm) and focused to an area of 5 μm in the full width at half maximum. From the filter transmittance data [28], the FEL peak fluence was estimated to be 2×10^9 photons/μm^2. NIR pulses with a wavelength of $\lambda = 800$ nm and pulse duration of 33 fs were focused to a focal size of 110 μm and overlapped with the FEL beam at a crossing angle of 0.5°. The arrival timing jitter between the FEL and the NIR pulses was determined using a timing monitor tool [22,23]. The jitter correction procedure was applied to the dataset [Figs. 1(b) and 2]. Xe clusters were produced via supersonic expansion of Xe gas at 0.1-MPa stagnation pressure and room temperature through a nozzle with a diameter

of 200 μm and a half angle of 15°. The average cluster size was estimated to be approximately 200 atoms according to the scaling law [29]. The kinetic-energy spectra of the emitted electrons were measured using a velocity map imaging (VMI) spectrometer [26]. The VMI images were normalized by the number of shots and background subtracted. The electron kinetic-energy spectra were then reconstructed from the acquired two-dimensional VMI images via Abel inversion using the PYABEL library [30].

B. Numerical modeling

1. Analytical model

To interpret the time evolution of the photoelectron spectra, we employed numerical modeling based on the multistep ionization scheme presented in the literature [31]. Note that our calculation does not consider the dynamics of the NIR-induced nanoplasmas. Instead, the dynamics was modeled by assuming different initial atomic coordinates in the clusters at the time of FEL irradiation. The photoionization of the $4d$, $5s$, and $5p$ electrons was considered with the atomic photoionization cross sections at $h\nu = 135$ eV. We assumed that $4d$ photoionization is always followed by a single Auger electron emission and that the ejected photo- and Auger electrons leave the vicinity of the cluster before the subsequent ionization event. Note that we neglected secondary ionization processes by inelastic collisions between the electrons and the atoms/ions. Considering the mean free path of electrons [32], it is a good approximation at the late stage of the neutral core expansion, which will be the subject of Sec. III C. The ejected electrons lose their energies due to the Coulomb potential of the previously produced ions. The kinetic energy of the released electrons was approximated by considering the average Coulomb potential $\langle \phi \rangle$ within a uniformly charged sphere,

$$\langle \phi(r) \rangle = \frac{Q}{4\pi\epsilon_0 R} \left(\frac{3}{2} - \frac{\langle r^2 \rangle}{2R^2} \right) \tag{1}$$

$$= \frac{Q}{4\pi\epsilon_0 R} \frac{6}{5}, \tag{2}$$

where e is the elementary charge, Q is the total charge, ϵ_0 is the vacuum permittivity, and R is the cluster radius. Here, the averaging procedure neglects the spatial variation of the potential within the cluster, however, our modeling provides spectra that are sufficiently precise to facilitate reasonable comparison with the experimental results. The average kinetic-energy E_k of $4d$ photoelectrons released from neutral atoms is approximated as follows:

$$E_k(n) = h\nu - I_p - e\langle \phi(r) \rangle \tag{3}$$

$$= h\nu - I_p - n \, \Delta E_k, \tag{4}$$

$$\Delta E_k = \frac{e^2}{4\pi\epsilon_0 R} \frac{6}{5} \left(2 + \frac{\sigma_{5s+5p}}{\sigma_{4d}} \right), \tag{5}$$

where n is the $4d$ ionization step, I_p is the Xe $4d$ ionization potential, σ_{4d} and σ_{5s+5p} are $4d$ and outershell ($5s$ and $5p$) photoabsorption cross sections. Equation (4) indicates a photoelectron energy shift that is proportional to the step n with a constant of proportionality of ΔE_k. The resulting
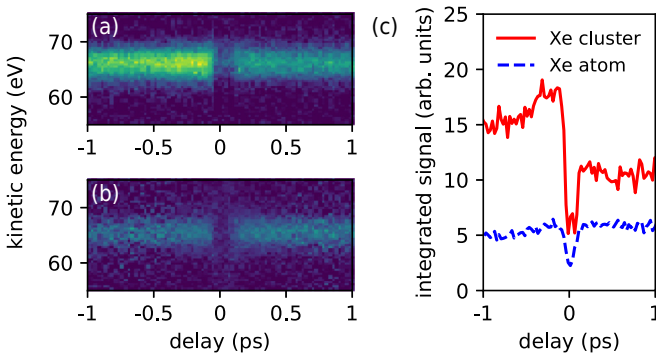

FIG. 2. The delay dependence of the Xe $4d$ photoelectron yields. (a) Pump-probe electron spectra of Xe clusters around the $4d$ photoelectron peak. The baseline from the thermal contribution from NIR-induced nanoplasma was subtracted. (b) Pump-probe electron spectra for atomic Xe. (c) Comparison of the $4d$ photoelectron yield between Xe clusters and atomic Xe.
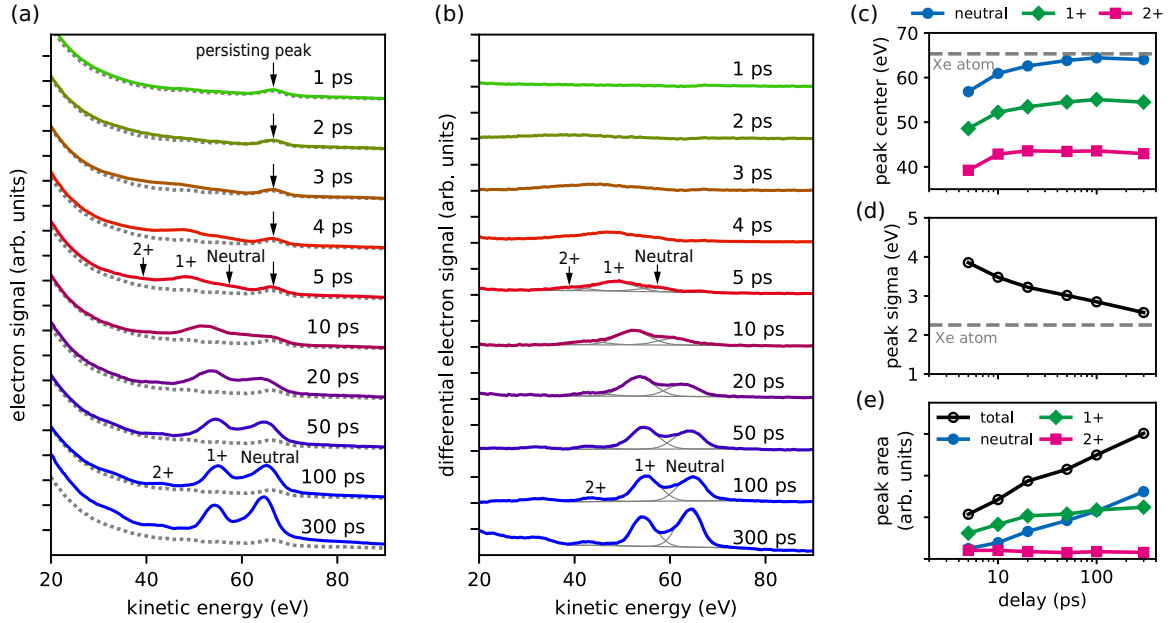
FIG. 3. Pump-probe photoelectron spectra of Xe clusters at NIR peak intensity of 1.5×10^{14} W/cm^2. (a) Raw pump-probe photoelectron spectra of Xe clusters. The dotted lines indicate the baseline corresponding to the broad thermal contribution from NIR-irradiated clusters and persisting photoelectron signal. (b) Photoelectron spectra after subtraction of the baseline. The photoelectron peaks were fitted with Gaussian functions (gray thin lines). (c) Photoelectron peak center positions, (d) peak width, and (e) peak area.

$4d$ photoelectron kinetic-energy distribution $y_{\text{model}}(E)$ can be expressed as follows:

$$y_{\text{model}}(E) = \sum_{n=0}^{n_{\max}} F(n)\delta[E - E_k(n)], \quad (6)$$

$$F(n) = \left(1 - \frac{1}{N_0}\right)^{\left(1 + \frac{\sigma_{5s+5p}}{\sigma_{4d}}\right)n}. \quad (7)$$

Here, $n_{\max} = N_0 f \sigma_{4d}$ is the maximum ionization step (N_0 is the number of atoms in the cluster, f is the beam fluence). $F(n)$ accounts for the decrease in neutral atoms in the cluster with the increasing ionization step. We then take the continuous limit of Eq. (6) and obtain the following formula:

$$y_{\text{model}}(E) = \begin{cases} \frac{F[n(E)]}{\Delta E_k}, & (h\nu - I_p - n_{\max}\Delta E_k < E \leqslant h\nu - I_p), \\ 0, & (\text{otherwise}), \end{cases} \quad (8)$$

$$n(E) = \frac{h\nu - I_p - E}{\Delta E_k}. \quad (9)$$

Equation (8) suggests the emergence of a plateau at the low-energy side of the atomic photoline, which agrees with the previous simulation results [31,33]. According to Eqs. (2) and (5), the height of the plateau is proportional to the cluster radius, whereas its length is inversely proportional to the radius when one assumes a constant N_0 (see Fig. 4). At the final step, peak broadening due to the spin-orbit splitting and bandwidth of the FEL beam was considered. The effects were included by summing the spectra in Eq. (8) for different values of I_p and $h\nu$. We assumed $I_p^{5/2} = 67.5$ eV for $4d_{5/2}^{-1}$ photoelectrons and $I_p^{3/2} = 69.5$ eV for $4d_{3/2}^{-1}$ photoelectrons with an intensity ratio of 3:2. In addition, the spectral bandwidth of the FEL beam was assumed to be $\Delta\lambda/\lambda = 0.02$ [24].

2. XMDYN *simulation*

In addition to the analytical approach, the photoelectron spectra of FEL-irradiated Xe clusters were calculated with XMDYN [34–38], a computer simulation software for modeling dynamics of finite systems induced by intense x rays. XMDYN treats real-space dynamics of classical particles (atoms, ions, and electrons) and excitation and relaxation processes (photoionization, Auger decay, fluorescense emission, electron-ion impact ionization, and electron-ion recombination) [35]. XMDYN has been successfully employed for modeling dynamics of rare-gas clusters irradiated by FEL [39,40]. The cross sections and rates of photoionization and innershell relaxations are calculated with the XATOM code [35,37] on the fly. Further details about the codes can be found in Refs. [34–38]. Note that the employed version of XATOM omits spin-orbit coupling [39], and the calculation of photo- and Auger elec-
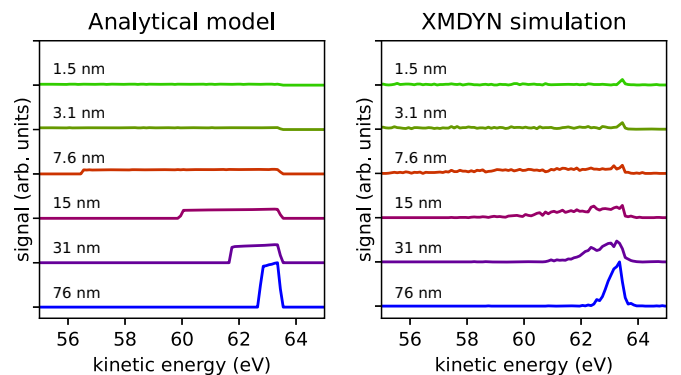

FIG. 4. Calculated photoelectron spectra of Xe$_{147}$ clusters with the analytical model and XMDYN simulation. The FEL fluence corresponds to a photoabsorption probability of 0.12 photons/atom.

tron energies are less accurate for heavy elements [39]. Our XMDYN simulation is based on the parameters described in Ref. [39]. An icosahedral Xe cluster with the ground-state electronic configuration was assumed as the initial structure. The XMDYN simulation was performed at 20 fluence values. At each fluence value, 96 random trajectories were propagated with a step size of 1 as up to 1.5 ps after the FEL pulse. The kinetic energies of all emitted electrons were used to construct the photoelectron spectra.

3. Focal volume effect

We performed analytical and XMDYN calculations that consider the intensity distribution of the FEL beam within the interaction region. Here, we assumed a Gaussian beam profile corresponding to the experimental peak fluence f_{peak}, pulse duration, and focal size. The spatial distribution of the fluence $f(r, z)$ is given as follows:

$$f(r, z) = f_{peak} \left(\frac{\omega_0}{\omega(z)} \right)^2 \exp \left(-\frac{2r^2}{\omega^2(z)} \right), \qquad (10)$$

$$\omega(z) = \omega_0 \sqrt{1 + (z/z_R)^2}, \qquad (11)$$

where ω_0 is the waist radius, and $z_R = \pi \omega_0^2 / \lambda$ is the Rayleigh length. In the present experimental setup, the Rayleigh length is long enough compared to the spatial cluster distribution, thus, we neglected the intensity variation along the beam propagation direction and only considered the two-dimensional cross section of the beam profile at $z = 0$. The photoelectron spectra were summed with weights corresponding to the real-space volume.

III. RESULTS AND DISCUSSIONS

A. FEL-only and NIR-only photoelectron spectra

Figure 1(a) shows the electron kinetic-energy spectra from Xe clusters irradiated by the NIR pulse, by the FEL pulse, and from the isolated Xe atoms irradiated by the FEL pulse. As can be seen, the NIR-only cluster spectrum exhibits a broad kinetic-energy distribution, which indicates the formation of nanoplasmas in the clusters.

The FEL-only spectra of the Xe clusters and atomic Xe exhibit prominent $4d$ photoelectron peaks at ~66 eV. Note that the slight shift of the $4d$ photoelectron peak in the cluster spectrum is explained by the polarization screening effect [41]. The atomic spectrum also exhibits small peaks arising from Auger decay subsequent to the $4d$ innershell ionization (28–36 eV) and $4d$ photoionization of doubly charged Auger final states (43–51 eV). The cluster spectrum also exhibits an increase in the baseline at the low-energy side of the $4d$ photoelectron peak (this is absent in the atomic spectrum). The baseline is explained by electron energy loss due to the developing Coulomb potential in the multistep ionization scheme [31]. At the present FEL fluence, the $4d$ photoabsorption probability is up to 1.0 photons/atom, which corresponds to multiple ionization and high ionization frustration in the cluster. The multistep ionization process yields a characteristic plateau at the low-energy part of the electron spectrum [31], which is comparable to the present cluster spectrum. In addition, inelastic collisions between photoelectrons and atoms/ions in the clusters can also contribute to the

signal at the low-energy side of the photoelectron peak. In the analysis of the pump-probe data, we focus on the delay-dependent behavior of the prominent $4d$ photoelectron peak, which is assumed to correspond to the photoelectrons that escaped from the cluster without losing significant energies.

B. Pump-probe photoelectron spectra

Figure 1(b) shows the pump-probe electron spectra of Xe clusters at the time delays $t = \pm 0.5$ ps. In the pump-probe spectra, the $4d$ photoelectron peaks from the probe FEL pulses appear at the tail of the broad thermal contribution from the NIR-irradiated clusters. By comparing the two spectra, an enhancement of the thermal contribution at the negative delay (i.e., when FEL arrives early) can be observed. This enhancement is caused by the efficient heating of the clusters ionized by the first FEL pulse with the second NIR laser pulse [42]. The baseline was fitted with three-order polynomials and subtracted from the spectra.

Figure 2(a) shows the cluster spectra after subtraction of the baseline, and Fig. 2(b) shows the spectra of the atomic Xe. The integrated photoelectron yields are given in Fig. 2(c). As shown, the integrated yields exhibit three prominent delay-dependent features, which are discussed in detail as follows. First, the cluster and atomic spectra exhibit dips at $t = 0$ ps, which is explained by the so-called photoelectron sidebands [43] that emerge at the wings of the photoelectron peak when the FEL and NIR pulses overlap temporally. At the given NIR laser intensity, the higher-order nonlinear interaction is prominent, which results in a significant reduction of the photoelectron yield [27] integrated around the peak (60–71 eV). Second, the photoelectron yield in the cluster spectra exhibits a steplike decrease at $t = 0$. Note that this is absent in the atomic spectra. This reduction of the photoelectron yield indicates the trapping of photoelectrons in the nanoplasma due to the emergence of Coulomb potential. Third, the photoelectron yield from clusters persists at a nonzero value at $t > 0.1$ ps. Here, the peak is assumed to originate, at least, partially from the condensed clusters because the peak position is shifted to the high-energy side compared to the $4d$ photoline of the atomic Xe. The persisting photoelectron signal suggests the existence of clusters where photoemission is not suppressed. The persisting peak likely originates from clusters that were off the NIR laser focus in the interaction region [44]. In our experimental setup, the NIR laser beam overlapped the FEL beam with a crossing angle of $0.5°$, which resulted in a nonuniform intensity distribution along the FEL beam axis.

In the following, we investigate the electron spectra at longer time delays in order to discuss the expansion and disintegration dynamics of nanoplasmas. Figure 3(a) shows the raw pump-probe photoelectron spectra at time delays $1 \leqslant t \leqslant 300$ ps. The raw spectra exhibit photoelectron peaks at the tail of the broad kinetic-energy distribution from NIR-irradiated clusters. In addition, there is a persisting peak at 66 eV, and this persisting peak does not shift with the delay and has a nearly constant intensity at $t \leqslant 5$ ps. As mentioned above, the persisting peak most likely originates from the clusters placed off the NIR focus and partially from the uncondensed Xe atoms. To offset the broad thermal contribution and persisting

photoelectron signals, the sum of the NIR-only spectrum y_{IR} and FEL-only spectrum y_{FEL} multiplied by a factor c was subtracted from the pump-probe spectra y_{IR+FEL} as follows:

$$y_{diff} = y_{IR+FEL} - y_{IR} - cy_{FEL}. \qquad (12)$$

Here, $c \approx 0.6$ was determined such that the persisting $4d$ photoelectron peak is offset in the differential spectra.

Figure 3(b) shows the differential electron spectra of Xe_{200} after baseline subtraction. The spectra exhibit $4d$ photoelectron peaks evolving with the time delay. The three pronounced peaks at the longer delays correspond to the $4d$ photoionization of neutral, singly charged, and doubly charged Xe atoms/ions, respectively. Here, the photoelectron peaks were fitted with Gaussian functions, and the results are shown in Figs. 3(c)–3(e). For successful convergence of the fitting procedure, fixed peak widths were assumed for the three peaks corresponding to the different charge states. As can be seen, the peak positions shift to high energies over time, and the position of the neutral Xe peak converges to the $4d$ photoline of the atomic Xe. In addition, the peak width exhibits a systematic decrease with the time delay and approaches that of the atomic Xe. Both of these delay-dependent behaviors suggest the disintegration of the nanoplasmas into ionic and atomic fragments, which corroborates with the scenario proposed in previous studies [3]. Quantitatively, the results are comparable to those of a numerical simulation of NIR-irradiated Ar_{923} clusters at a similar laser intensity of 1.4×10^{14} W/cm^2 [45].

Next, we discuss the delay dependence of the photoelectron yields at $1 \leqslant t \leqslant 300$ ps. As shown in Fig. 3(d), the total $4d$ photoelectron yield exhibits a steady increase over the measured delay range. Here, to understand the delay dependence, we formulate the total electron yield Y_{tot} as follows:

$$Y_{tot} \propto \sum_{i=0}^{N} f\sigma_{q_i} p_i, \qquad (13)$$

where f is the fluence of the incident FEL beam, σ_{q_i} is the $4d$ photoabsorption cross section for charge species q_i, N is the number of atoms and ions, and p_i is the probability that a photoelectron can escape from the cluster without losing a significant amount of energy. Considering the weak dependence of σ_{q_i} on the charge state q_i [46] and conservation of the total number of atoms and ions, the increase in y_{tot} can only be explained by the increase in p_i. In fact, the increase in p_i reflects the fragmentation stage of the clusters. In dense clusters, the escape probability p_i is reduced by the presence of electron energy loss mechanisms, i.e., the multistep ionization and inelastic-scattering processes. As the cluster expands and disintegrates into atomic fragments after laser excitation, both effects vanish because the electron energy-loss processes only occur in dense aggregates [refer to the cluster and atomic spectra in Fig. 1(a)]. The cluster rarefaction causes the increase in p_i and the total photoelectron yield.

Furthermore, the time-dependent photoelectron yields provide insights into the charge-state-specific fragmentation of the laser-heated clusters. As shown in Fig. 3(e), the photoelectron yields from both singly and doubly charged Xe ions reach plateaus within 10 ps. In contrast, the photoelectron
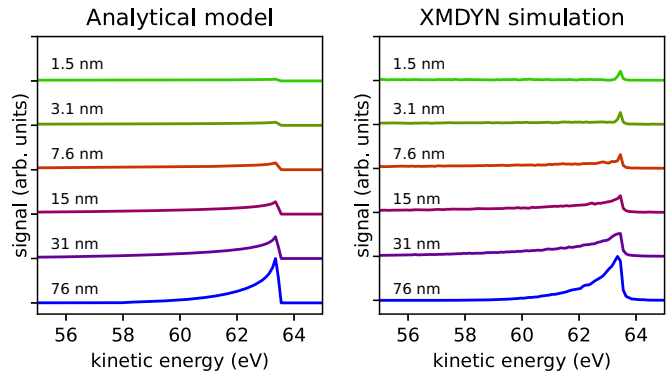

FIG. 5. Calculated photoelectron spectra of Xe_{147} clusters with the analytical model and XMDYN software. The spatial intensity distribution of the FEL beam was taken into account.

yield from neutral atoms shows a steady increase over several tens of picoseconds. These observations are well explained by the two-step fragmentation picture [13], i.e., the rapid expansion of surface ions and subsequent slow expansion of the neutral core. Here, we verify this picture in terms of both the present and previous findings. Upon strong laser excitation of the cluster and trapping the electrons in the nanoplasma, the surface ions undergo rapid expansion. This ion explosion results in an increase in the number of photoelectrons emitted from the outgoing ions. Consequently, the photoelectron yield reaches a plateau on the timescale of the ion explosion. The typical timescale of the ion explosion is 1 ps [4], which is in reasonable agreement with our experimental results. Meanwhile, efficient recombination of the excited electrons leads to the formation of the neutral cluster core [8,9,12–14]. Our observations suggest that the expansion and rarefaction of the neutral core proceed on a timescale of tens of picoseconds, which results in increased photoelectron yield from the neutral atoms. The slow fragmentation of cluster core is reminiscent of the results of time-resolved imaging of NIR-induced plasma in large Xe nanoparticles (radius > 100 nm) [13]. The present results confirm the charge neutrality of the residual cluster core and suggest the applicability of the scenario of the two-step fragmentation to small clusters in the present case.

C. Comparison with numerical modeling

In the following, we evaluate the speed of the neutral core expansion from the increased photoelectron yield. To connect the photoelectron yield to the expansion stage of the neutral core, the photoelectron spectra from the expanding neutral core were calculated with the analytical model and XMDYN simulation. Figure 4 shows the calculated photoelectron spectra of neutral Xe_{147} clusters at an FEL fluence corresponding to a photoabsorption probability of 0.12 photons/atom. Here, we assumed a single binding energy ($I_p = 71.6$ eV), monochromatic FEL beam ($h\nu = 135$ eV), and photoionization cross sections calculated with the XATOM code for comparison between the analytical model and the XMDYN results. Both series of spectra exhibit growth of the $4d$ photoelectron peak along with the core expansion, and the analytical spectra approximate the spectral shape of those simulated with XMDYN. Note that the main source of the
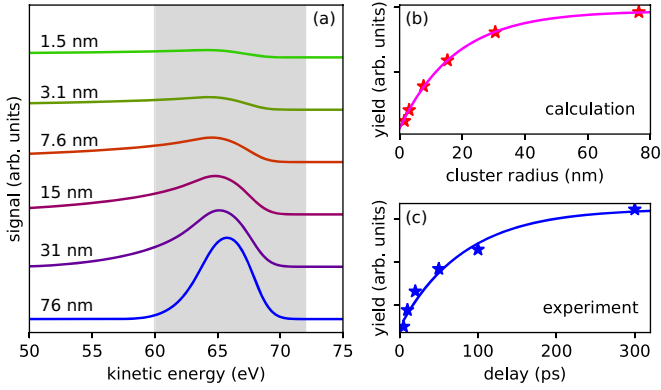
FIG. 6. (a) Calculated photoelectron spectra of Xe_{147} clusters with the analytical model at various cluster radii. Photoelectron peak broadening due to the spin-orbit splitting and the FEL bandwidth were additionally considered. (b) Photoelectron yield of the calculated spectra integrated over the shaded area in (a). (c) Experimental photoelectron yields from neutral atoms reproduced from Fig. 3(e). The calculated and experimental photoelectron yields are fitted with asymptotic exponential curves.

difference is the statistical fluctuations of the number of absorbed photons in the XMDYN simulation. Even better agreements were obtained after integrating the spectra at different FEL intensities with weights corresponding to the real-space volume (Fig. 5). These results demonstrate the effectiveness of our model despite several approximations.

We now compare the analytical photoelectron spectra with the experimental data. To realize a better comparison with the experimental spectra, photoelectron peak broadening due to the spin-orbit splitting and the FEL bandwidth were additionally considered. Figure 6(a) shows the simulated photoelectron spectra at various expansion stages of the neutral core. The increase in the $4d$ photoelectron signal was well reproduced in the calculation, which supports the considerations in the previous subsection. Note that this calculation does not include the transient peak shift that was observed experimentally due to neglecting the outgoing ions. The integrated photoelectron yield [Fig. 6(b)] was fitted with an asymptotic exponential function,

$$Y_{\text{calc}} = -(B - A) \exp\left(-\frac{R - R_0}{L}\right) + B, \quad (14)$$

where A and B are the initial and final yields, respectively, R_0 is the initial core radius, and L is the characteristic length dimension over which the neutral core should expand to cause the increase in the photoelectron yield. The fitting procedure yielded the characteristic length scale L of 20 nm. Then, to extract the timescale of the neutral core expansion from the experimental data, the delay-dependent photoelectron yield from neutral Xe [Fig. 6(c)] was fitted with a similar asymp-

totic exponential curve,

$$Y_{\text{exp}} = -(D - C) \exp\left(-\frac{t}{\tau}\right) + D. \quad (15)$$

Here, C and D are the initial and final photoelectron yields, respectively, and τ is the characteristic timescale. The resulting characteristic timescale was $\tau = 80$ ps. By combining the simulation and experimental results, we obtained the speed of the neutral core expansion of approximately $L/\tau = 200$ m/s. The expansion speed is more than one order of magnitude less than the reported speed of ions ejected from NIR laser-heated clusters at a similar laser intensity [10]. In fact, the obtained speed is on the order of the typical value of gaseous sound speed or the velocity of molecules (cf. the sound speed of Xe at 300 K is 180 m/s [47]). This agreement implies that the neutral core expansion could be understood as neutral gas expansion into vacuum. This consideration would be reasonable under the assumption that the neutral core expansion proceeds after full charge neutralization. The present results also demonstrate that surface ions and electrons carry the vast majority of energy absorbed in the cluster whereas leaving a small fraction of energy to the neutral core. This highly effective energy transfer to the surface ions is presumably a key mechanism in the production of high-energy ions [14].

IV. CONCLUSION

We investigated the expansion dynamics of NIR-induced nanoplasmas using TRPES with a short-wavelength FEL. The delay-dependent photoelectron spectra provide direct information on the transient electron energy levels in expanding nanoplasmas, which supports the scenario proposed in previous studies [3]. As an important step forward, we have identified the expansion of the neutral cluster core on tens of picosecond timescale, which is likely similar to that of neutral gas expansion into the vacuum. We believe that these findings are potentially applicable to nanoplasma dynamics in other excitation regimes (e.g., x-ray and ultraviolet), if we consider the similarity of the long-term dynamics of the nanoplasmas produced in such regimes. The findings of this paper provide a comprehensive picture of the fragmentation of intense laser-irradiated matter. These findings will contribute to improving theoretical modeling and the design of experiments and applications using intense lasers.

[1] T. Ditmire, J. W. G. Tisch, E. Springate, M. B. Mason, N. Hay, R. A. Smith, J. Marangos, and M. H. R. Hutchinson, Nature (London) **386**, 54 (1997).

[2] M. Lezius, S. Dobosz, D. Normand, and M. Schmidt, Phys. Rev. Lett. **80**, 261 (1998).

[3] T. Fennel, K.-H. Meiwes-Broer, J. Tiggesbäumker, P.-G. Reinhard, P. M. Dinh, and E. Suraud, Rev. Mod. Phys. **82**, 1793 (2010).

[4] J. W. G. Tisch, N. Hay, K. J. Mendham, E. Springate, D. R. Symes, A. J. Comley, M. B. Mason, E. T. Gumbrell, T. Ditmire, R. A. Smith, J. P. Marangos, and M. H. R. Hutchinson, Nucl. Instrum. Methods Phys. Res., Sect. B **205**, 310 (2003).

[5] T. Fennel, T. Döppner, J. Passig, C. Schaal, J. Tiggesbäumker, and K.-H. Meiwes-Broer, Phys. Rev. Lett. **98**, 143401 (2007).

[6] Y. L. Shao, T. Ditmire, J. W. G. Tisch, E. Springate, J. P. Marangos, and M. H. R. Hutchinson, Phys. Rev. Lett. **77**, 3343 (1996).

[7] T. Döppner, T. Fennel, T. Diederich, J. Tiggesbäumker, and K. H. Meiwes-Broer, Phys. Rev. Lett. **94**, 013401 (2005).

[8] M. Hoener, C. Bostedt, H. Thomas, L. Landt, E. Eremina, H. Wabnitz, T. Laarmann, R. Treusch, A. R. B. de Castro, and T. Möller, J. Phys. B: At. Mol. Opt. Phys. **41**, 181001 (2008).

[9] L. Schroedter, M. Müller, A. Kickermann, A. Przystawik, S. Toleikis, M. Adolph, L. Flückiger, T. Gorkhover, L. Nösel, M. Krikunova, T. Oelze, Y. Ovcharenko, D. Rupp, M. Sauppe, D. Wolter, S. Schorb, C. Bostedt, T. Möller, and T. Laarmann, Phys. Rev. Lett. **112**, 183401 (2014).

[10] B. Schütte, T. Oelze, M. Krikunova, M. Arbeiter, T. Fennel, M. J. J. Vrakking, and A. Rouzée, New J. Phys. **17**, 033043 (2015).

[11] B. Schütte, T. Oelze, M. Krikunova, M. Arbeiter, T. Fennel, M. J. J. Vrakking, and A. Rouzée, J. Phys. B: At., Mol. Opt. Phys. **48**, 185101 (2015).

[12] B. Schütte, F. Campi, M. Arbeiter, T. Fennel, M. J. J. Vrakking, and A. Rouzée, Phys. Rev. Lett. **112**, 253401 (2014).

[13] L. Flückiger, D. Rupp, M. Adolph, T. Gorkhover, M. Krikunova, M. Müller, T. Oelze, Y. Ovcharenko, M. Sauppe, S. Schorb, C. Bostedt, S. Düsterer, M. Harmand, H. Redlin, R. Treusch, and T. Möller, New J. Phys. **18**, 043017 (2016).

[14] D. Rupp, L. Flückiger, M. Adolph, T. Gorkhover, M. Krikunova, J. P. Müller, M. Müller, T. Oelze, Y. Ovcharenko, B. Röben, M. Sauppe, S. Schorb, D. Wolter, R. Mitzner, M. Wöstmann, S. Roling, M. Harmand, R. Treusch, M. Arbeiter, T. Fennel et al., Phys. Rev. Lett. **117**, 153401 (2016).

[15] T. Gorkhover, S. Schorb, R. Coffee, M. Adolph, L. Foucar, D. Rupp, A. Aquila, J. D. Bozek, S. W. Epp, B. Erk, L. Gumprecht, L. Holmegaard, A. Hartmann, R. Hartmann, G. Hauser, P. Holl, A. Hömke, P. Johnsson, N. Kimmel, K.-U. Kühnel et al., Nat. Photonics **10**, 93 (2016).

[16] W. Ackermann, G. Asova, V. Ayvazyan, A. Azima, N. Baboi, J. Bähr, V. Balandin, B. Beutner, A. Brandt, A. Bolzmann, R. Brinkmann, O. I. Brovko, M. Castellano, P. Castro, L. Catani, E. Chiadroni, S. Choroba, A. Cianchi, J. T. Costello, D. Cubaynes et al., Nat. Photonics **1**, 336 (2007).

[17] P. Emma, R. Akre, J. Arthur, R. Bionta, C. Bostedt, J. Bozek, A. Brachmann, P. Bucksbaum, R. Coffee, F.-J. Decker, Y. Ding, D. Dowell, S. Edstrom, A. Fisher, J. Frisch, S. Gilevich, J. Hastings, G. Hays, P. Hering, Z. Huang et al., Nat. Photonics **4**, 641 (2010).

[18] D. M. Neumark, Annu. Rev. Phys. Chem. **52**, 255 (2001).

[19] R. J. Squibb, M. Sapunar, A. Ponzi, R. Richter, A. Kivimäki, O. Plekan, P. Finetti, N. Sisourat, V. Zhaunerchyk, T. Marchenko, L. Journel, R. Guillemin, R. Cucini, M. Coreno, C. Grazioli, M. Di Fraia, C. Callegari, K. C. Prince, P. Decleva, M. Simon et al., Nat. Commun. **9**, 63 (2018).

[20] F. Brauße, G. Goldsztejn, K. Amini, R. Boll, S. Bari, C. Bomme, M. Brouard, M. Burt, B. C. de Miranda, S. Düsterer, B. Erk, M. Géléoc, R. Geneaux, A. S. Gentleman, R. Guillemin, I. Ismail, P. Johnsson, L. Journel, T. Kierspel, H. Köckert et al., Phys. Rev. A **97**, 043429 (2018).

[21] S. Pathak, L. M. Ibele, R. Boll, C. Callegari, A. Demidovich, B. Erk, R. Feifel, R. Forbes, M. Di Fraia, L. Giannessi, C. S. Hansen, D. M. P. Holland, R. A. Ingle, R. Mason, O. Plekan, K. C. Prince, A. Rouzée, R. J. Squibb, J. Tross, M. N. Ashfold et al., Nat. Chem. **12**, 795 (2020).

[22] S. Owada, K. Nakajima, T. Togashi, T. Kayatama, and M. Yabashi, J. Synchrotron Radiat. **25**, 68 (2018).

[23] S. Owada, K. Nakajima, T. Togashi, T. Katayama, H. Yumoto, H. Ohashi, and M. Yabashi, J. Synchrotron Radiat. **26**, 887 (2019).

[24] S. Owada, K. Togawa, T. Inagaki, T. Hara, T. Tanaka, Y. Joti, T. Koyama, K. Nakajima, H. Ohashi, Y. Senba, T. Togashi, K. Tono, M. Yamaga, H. Yumoto, M. Yabashi, H. Tanaka, and T. Ishikawa, J. Synchrotron Radiat. **25**, 282 (2018).

[25] A. Niozu, N. Yokono, T. Nishiyama, H. Fukuzawa, T. Sakurazawa, K. Matsuda, T. Takanashi, D. You, Y. Li, T. Ono, T. Gaumnitz, M. Schöffler, S. Grundmann, S. Wada, P. Carpeggiani, W. Q. Xu, X. J. Liu, S. Owada, K. Tono, T. Togashi et al., J. Chem. Phys. **151**, 184305 (2019).

[26] H. Fukuzawa, K. Nagaya, and K. Ueda, Nucl. Instrum. Methods Phys. Res., Sect., A **907**, 116 (2018).

[27] S. Owada, M. Fushitani, A. Matsuda, H. Fujise, Y. Sasaki, Y. Hikosaka, A. Hishikawa, and M. Yabashi, J. Synchrotron Radiat. **27**, 1362 (2020).

[28] B. L. Henke, E. M. Gullikson, and J. C. Davis, At. Data Nucl. Data Tables **54**, 181 (1993).

[29] O. F. Hagena, Surf. Sci. **106**, 101 (1981).

[30] D. D. Hickstein, S. T. Gibson, R. Yurchak, D. D. Das, and M. Ryazanov, Rev. Sci. Instrum. **90**, 065115 (2019).

[31] C. Bostedt, H. Thomas, M. Hoener, E. Eremina, T. Fennel, K.-H. Meiwes-Broer, H. Wabnitz, M. Kuhlmann, E. Plönjes, K. Tiedtke, R. Treusch, J. Feldhaus, A. R. B. de Castro, and T. Möller, Phys. Rev. Lett. **100**, 133401 (2008).

[32] R. C. Wetzel, F. A. Baiocchi, T. R. Hayes, and R. S. Freund, Phys. Rev. A **35**, 559 (1987).

[33] M. Arbeiter and T. Fennel, New J. Phys. **13**, 053022 (2011).

[34] Z. Jurek, V. Lipp, N. Medvedev, R. Santra, S.-K. Son, B. Ziaja, XRAYPAC – a Software package for modeling x-ray-induced dynamics of matter, v. 4.01, CFEL, DESY (2021).

[35] Z. Jurek, S.-K. Son, B. Ziaja, and R. Santra, J. Appl. Crystallogr. **49**, 1048 (2016).

[36] Z. Jurek, G. Faigel, and M. Tegze, Eur. Phys. J. D **29**, 217 (2004).

[37] S.-K. Son, L. Young, and R. Santra, Phys. Rev. A **83**, 033402 (2011).

[38] B. F. Murphy, T. Osipov, Z. Jurek, L. Fang, S.-K. Son, M. Mucke, J. H. D. Eland, V. Zhaunerchyk, R. Feifel, L. Avaldi,

P. Bolognesi, C. Bostedt, J. D. Bozek, J. Grilj, M. Guehr, L. J. Frasinski, J. Glownia, D. T. Ha, K. Hoffmann, E. Kukk *et al.*, Nat. Commun. **5**, 4281 (2014).

[39] T. Tachibana, Z. Jurek, H. Fukuzawa, K. Motomura, K. Nagaya, S. Wada, P. Johnsson, M. Siano, S. Mondal, Y. Ito, M. Kimura, T. Sakai, K. Matsunami, H. Hayashita, J. Kajikawa, X.-J. Liu, E. Robert, C. Miron, R. Feifel, J. P. Marangos *et al.*, Sci. Rep. **5**, 10977 (2015).

[40] Y. Kumagai, Z. Jurek, W. Xu, V. Saxena, H. Fukuzawa, K. Motomura, D. Iablonskyi, K. Nagaya, S. Wada, Y. Ito, T. Takanashi, S. Yamada, Y. Sakakibara, T. N. Hiraki, T. Umemoto, M. Patanen, J. D. Bozek, I. Dancus, M. Cernaianu, C. Miron *et al.*, J. Phys. B: At., Mol. Opt. Phys. **54**, 044001 (2021).

[41] O. Björneholm, F. Federmann, F. Fössing, and T. Möller, Phys. Rev. Lett. **74**, 3017 (1995).

[42] B. Schütte, M. Arbeiter, A. Mermillod-Blondin, M. J. J. Vrakking, A. Rouzée, and T. Fennel, Phys. Rev. Lett. **116**, 033001 (2016).

[43] T. E. Glover, R. W. Schoenlein, A. H. Chin, and C. V. Shank, Phys. Rev. Lett. **76**, 2468 (1996).

[44] A. Niozu, Y. Kumagai, H. Fukuzawa, N. Yokono, D. You, S. Saito, Y. Luo, E. Kukk, C. Cirelli, J. Rist, I. Vela-Pérez, T. Kameshima, Y. Joti, K. Motomura, T. Togashi, S. Owada, T. Katayama, K. Tono, M. Yabashi, L. Young *et al.*, Phys. Rev. X **11**, 031046 (2021).

[45] B. Schütte, M. Arbeiter, T. Fennel, G. Jabbari, A. I. Kuleff, M. J. J. Vrakking, and A. Rouzée, Nat. Commun. **6**, 8596 (2015).

[46] J. B. West, J. Phys. B: At., Mol. Opt. Phys. **34**, R45 (2001).

[47] J. J. Hurly, J. W. Schmidt, S. J. Boyes, and M. R. Moldover, Int. J. Thermophys. **18**, 579 (1997).